CYBERNETICS AND PHYSICS, VOL. 3, NO. 2, 2014 , 55–61

# DATA PROCESSING IN NUCLEAR MEDICINE

**Elena Kotina**
Saint Petersburg State University
Russia
ekotina123@mail.ru

**Dmitri Ovsyannikov**
Saint Petersburg State University
Russia

**Viktor Ploskikh**
Saint Petersburg State University
Russia

**Viktor Latypov**
Saint Petersburg State University
Russia

**Andrey Babin**
Saint Petersburg State University
Russia

**Alexander Shirokolobov**
Saint Petersburg State University
Russia

**Abstract**

Nuclear medicine is a branch of medical science involving the application of radioactive substances in the diagnosis and treatment of disease. The data processing in nuclear medicine is very important for the estimation of the functional status of the various organs and body systems. Single-photon emission computed tomography (SPECT) data processing is considered in this work. The main stages of data processing are studied. The purpose of this study is to develop and apply mathematical methods for SPECT data processing

**Key words**

Single-photon emission computed tomography, reconstruction, motion correction, data processing

## 1 Introduction

Data processing has been involved the following main stages: data correction, tomography reconstruction, three-dimensional visualization, functional images construction, mathematical modeling of studied processes and calculation of diagnostic parameters. Mathematical modeling of static, dynamic and gated processes in nephrology, osteology, endocrinology and cardiology is considered for quantitative analysis in papers [Balykina et al., 2014; Kotina, 2012; Kotina and Ploskikh, 2012]. In this paper we consider motion correction, reconstruction and functional images construction in cardiology.

## 2 Motion Correction

Motion correction problems exist for diagnostic studies [Germano et al., 1993], as well as for planning radiation therapy [Elizarova, Ovsyannikov and Cheremisin, 2007].

The finding and correction of the patient motion are one of the most important step of the processing of radionuclide studies. Even small dislocation of the patient or of the target organ during the process of data collection may affect to the accuracy of diagnostic results. It is impossible to avoid the position changing of the patient or its target organs during data acquisition.

### 2.1 Method of the Cross-correlation Function

The method of cross-correlation function is applied to determine and correct motion [Sarkar et al. , 2007]. It is based on the analysis of cross-correlation function defined for consecutive planar images.

Let introduce two coordinate systems. The moving system of coordinates $(x, y)$, associated with the detector, which rotates in a circular orbit around the center of fixed coordinate system $(x', y', z')$. This system associated with the gamma camera gantry (Fig. 1).

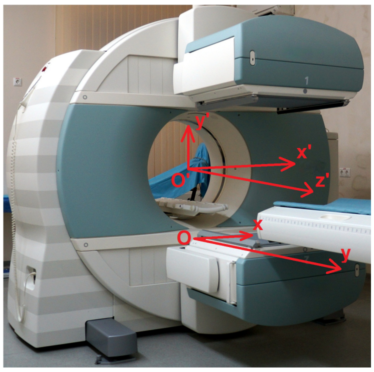

Figure 1. The coordinate systems. The moving system $(x, y)$. The fixed system $(x', y', z')$

The transverse motion is the position displacement of the examined organ parallel to the plane $(x', y')$, and a longitudinal — parallel to the axis $z'$.

We consider the correlation between the one frame and the next. The cross-correlation function for two consecutive frames with indices $k$ and $k + 1$ will have the form [Eisner et al., 1987]

$$fx_k = \sum_{j=1}^{n} C_{jk} C_{j+s,k+1}, -K \leqslant s \leqslant K, \quad (1)$$

$$fy_k = \sum_{i=1}^{n} D_{ik} D_{i+s,k+1}, -K \leqslant s \leqslant K, \quad (2)$$

where $K \in N$, $C_{j+s,k+1} = 0$, if $j+s < 1$ or $j+s > n$, and $D_{i+s,k+1} = 0$, if $i+s < 1$ or $i+s > n$, $C_{jk}$ and $D_{ik}$ — total profiles along the $Ox$ and $Oy$ axes respectively [Ovsyannikov, Kotina and Shirokolobov, 2013].

Formulas ( 1) and ( 2) represent a view of the cross-correlations function to determine transverse and longitudinal movements respectively.

## 2.2 SPECT

The camera turns around the patient, during the data collection of the SPECT. This fact must be taken into account for motion correction.

In the case when there is no patient motion, the trajectory of the point projection $(x', y', z')$ must be sinusoidal relative to the axis $Ox$ and the line relative to the axis $Oy$.

It is nessesary to determine the interval on the frames, before we start detection of the motion (Fig. 2).

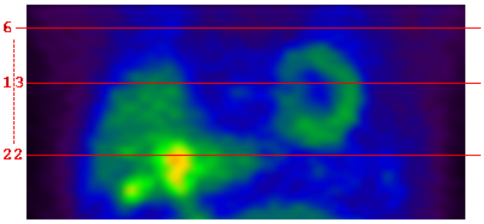

Figure 2. Interval selection

The sinogram and linogram [Kotina and Maximov, 2011] are built for the visual detection of displacement along the $Ox$ and $Oy$ axes respectively and futher correction by cross-correlation method.

The final value of the frame displacement is determined by the parabolic fitting of the peak of the cross-correlation function.

Figure 3 are shows the sinograms before and after motion correction.

## 2.3 Planar Imaging

During dynamic planar acquisition detector is stationary. A sequence of images with a fixed exposure is formed for each detector.

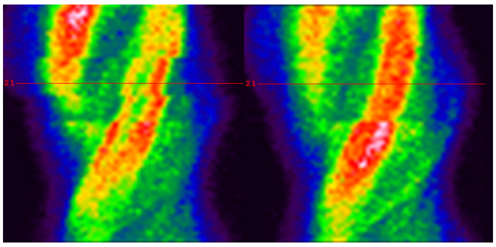

Figure 3. Sinogram before (left) and sinogram after (right) correction

In the case when there is no patient motion, the trajectory of the point projection $(x', y', z')$ must be lines relative to the axis $Ox$ and $Oy$.

With the purpose to increase the ratio signal-to-noise for the investigated organ, it is necessary to determine the area of interest, before we start detection of the motion (Fig. 4).

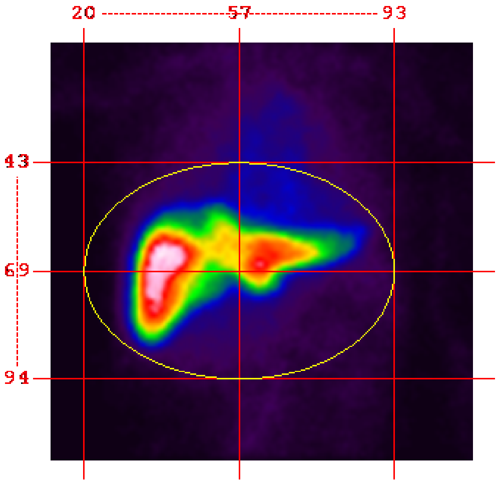

Figure 4. Determine the area of interest - the liver - for the subsequent motion correction

The linograms along the $Ox$ and $Oy$ axes are built for the visual detection of displacement along the $Ox$ and $Oy$ axes respectively.

Figure 5 are shows the linograms before and after motion correction.

The motion correction problem for dynamic planar imaging can be considered as problem of ROI contour correction in case of organ motion. It can take place under consideration of hepatobiliary scintigraphy dynamic planar imaging, for example, gallbladder contour position correction [Shirokolobov, 2014].

In static planar imaging, the data acquisition protocol needed to be exchanges from static to dynamic modality with purpose of application of the same motion-correction scheme.

We can note also that the use of the approache described in [Ovsyannikov and Kotina, 2012] can be helpful for the motion correction as well. These ap-

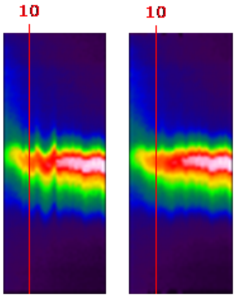

Figure 5. Linogram before (left) and linogram after (right) correction

proach is based on the determination of the velocity field and can be used for the solving of motion correction problems for radionuclide studies.

## 3 Reconstruction

The diagnostically important parameters in nuclear medicine are often calculated from the volumetric radoipharmaceutical density distribution function. The unknown distribution is calculated from the data acquired from SPECT device. The calculation process is known as tomographic reconstruction and it is a time-consuming and computationally intensive task.

### 3.1 Definitions

Let us recall the basic notation used in tomographic image reconstruction. Commonly used SPECT data acquisition model considers the tomographic device as a linear transformation from the volume space to the projection data space. The unknown radiopharmaceutical distribution density is denoted by $f(x, y, z)$. The SPECT device sums the influence of each volume point $(x, y, z)$ and outputs the data for each detector bin. The data for all the detectors is gathered in the vector $p_i$. The distribution density $f(x, y, z)$ samples are enumerated and denoted as a vector $f_j$. Fig. 6 shows the details of the acquisition process. On the left is the detector grid and on the right is the volumetric array of point where the distribution density function is sampled.

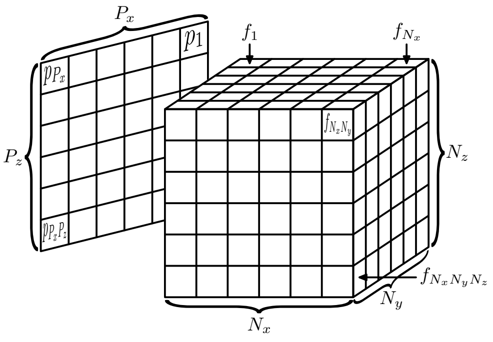

Figure 6. Discrete volume and detectors

The measurement process is expressed in the relation

$$p = Af. \tag{3}$$

Matrix $A$ is called the system response matrix (SRM) or the projection matrix. Its computation for SPECT is considered in details in [Dey and King, 2009]. The element of the projection matrix is the probability that a gamma quantum creation event in the cell $j$ is detected in the bin $i$. The probability is the product of a multiple factors. In this system we consider only the most important geometric factor which is proportional to the volume of intersection of the cell and visibilty cone of the $i$-th detector. The detector visibility cone is shown in Fig. 7.

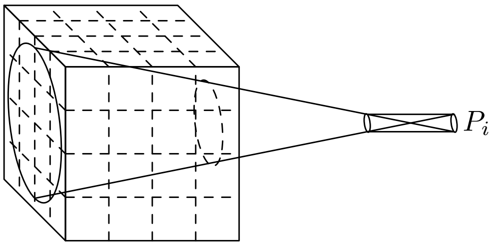

Figure 7. Visibility cone

To simplify the calculations we consider the planar case. The extension of the calculation to three dimensions is straightforward.

The two-dimensional slice and a typical grid detector arrangement shown in Fig. 8.

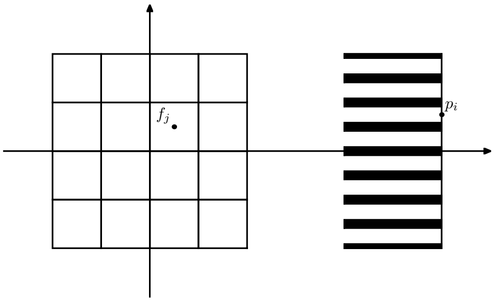

Figure 8. Null angle detector position

To calculate the intersection volume of the voxel and the visibility cone simple trigonometric considerations are used. First we calculate the solid angle $\varphi$ and divide it by $4\pi$, the area of a unit sphere, to get the geometric probability of a photon to get into the $i$-th detector. Then we check if the straight line from the voxel center to the detector center does not intersect the collimator. The detector visibility angle $\varphi$ is shown in Fig. 9.

The $dx$ and $dy$ are the horizontal and vertical distances from the voxel center to the detector bin center, $dp$ is

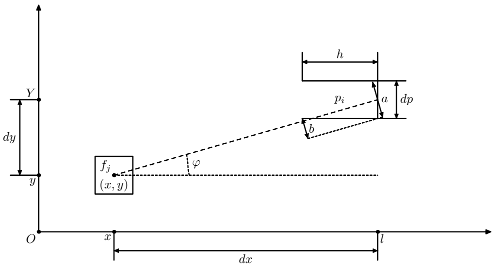

Figure 9. Detector visibility

the height of the detector and $p$ is the collimator thickness.

$$d = \sqrt{dx^2 + dy^2}, \quad a = \frac{dp \cdot dx}{d}, \quad b = \frac{h \cdot dy}{d},$$

Using these values the $\varphi$ angle is calculated. Finally, the matrix element $a_{ij}$ is calculated if the visibility angle is greater than zero.

$$\varphi = \frac{(a - kb)\, dp}{d^2}, \quad a_{ij} = \begin{cases} \frac{\varphi}{4\pi}, \varphi \geq 0, \\ 0, \varphi < 0. \end{cases}$$

## 3.2 Algorithms

Typical dimensions of the reconstructed image slice are large (up to 256x256 pixels) and the number of detectors is also large (64x64). To solve the system of equations (3) iterative methods are used. The most common algorithm is the Maximum Likelihood Expectance Maximization (MLEM) by Shepp and Vardi [Shepp and Vardi, 1982] and its modification, Ordered Subsets EM (OSEM) by Hudson and Larkin [Hudson and Larkin, 1994]. Single iteration of the algorithm consists of the following calculations:

$$f_{k+1} = f_k \frac{A^T \left(\frac{p}{Af}\right)}{A^T 1}.$$

The $T$ superscript denotes matrix transposition, 1 is the vector with all elements equal to 1. The division and multiplication are performed element-wise. The multiplication of matrix A and its transpose by the vectors f and p is performed according to the standard linear algebraic rules. One might note that the denominator is the vector with j-th element equal to the sum of A matrix components in the j-th row.

The single iteration of the MLEM algorithm consists of three basic operations:

Projection or the multiplication by A.

Backprojection or the multiplication by the transposed matrix A .

Correction element-wise multiplication of the image by the projection and backprojection ratio.

Third step of the iteration is easily parallelizable and takes less time compared to step 1 and 2. First two steps are essentially the same and consist only of the matrix by vector multiplication.

In our system a custom parallel implementation of MLEM using an OpenCL [Munshi, 2014] programming language is used for SPECT image reconstruction [Kotina, Latypov and Ploskikh, 2013]. This technology allows the program to run on any modern GPU from major manufacturers as nVidia, AMD and Intel. For 2D reconstruction of the image and a typical SPECT detector configuration it is possible to upload the whole system response matrix to the GPU memory using the Yale compression scheme also known as compressed row storage [Pissanetzky, 1984].

## 3.3 Results

The slices of the volumes reconstructed from SPECT data are shown in Fig. 10 and Fig. 11. The source data is acquired with the EFATOM SPECT scanner [Arlychev et al. 2009].

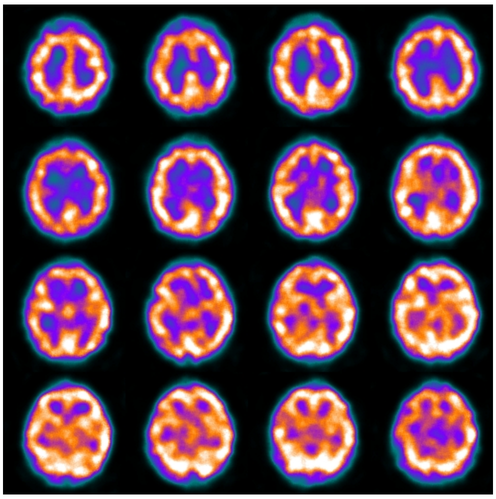

Figure 10. Slices of a SPECT brain scan.

## 4 Data Processing in Cardiology

Cardiology is one of the main medical areas of radionuclide methods and SPECT usage. Radionuclide methods in cardiac studies allow performing functional diagnostics of the cardiovascular system. One of the most needed tomographic methods is gated SPECT myocardial perfusion imaging (MPI). MPI is modern radionuclide method of investigation of the heart, which allows visualizing three-dimensional distribution of radiopharmaceuticals in myocardium at different time points of “representative” cardiac cycle. The functional images has been playing significant role in diagnostics.

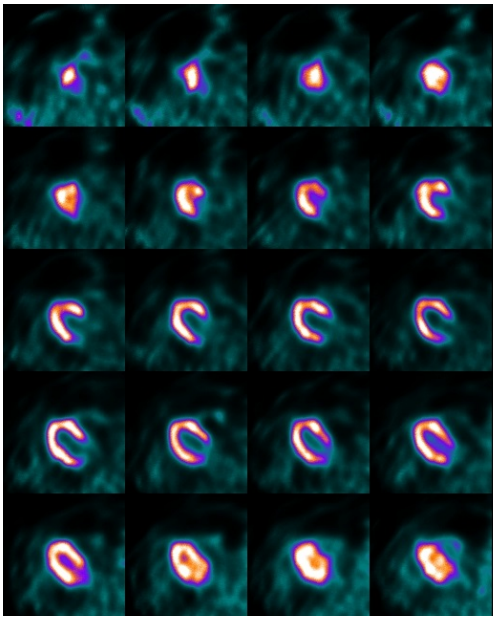

Figure 11. Slices of a SPECT heart scan.

### 4.1 Functional Images Construction

Algorithm of data processing of MPI studies allows defining physiologically meaningful indicators of perfusion and function of the heart was considered [Kotina, Ploskikh, and Babin, 2013]. Let consider in details the algorithm of functional images construction (phase images and parametric images of systolic and diastolic dyssynchrony) for measuring and visualizing ventricular dyssynchrony. The use of wavelet analysis method is proposed for the building of these functional images.

The functional images are constructed using Fourier analysis for comparative analysis. Phase analysis using Fourier harmonic functions has been developed for measuring left ventricular (LV) systolic dyssynchrony from gated SPECT MPI [Chen et al., 2005]. It is important that dyssynchrony as assessed by phase analysis can provide incremental prognostic information to other parameters measured from gated SPECT MPI such as perfusion and LV ejection fraction and predict response to cardiac resynchronization therapy [Ostroumov et al., 2011].

These functional images are represented as polar diagrams “bull eye” [Taylor and Grant, 2006], which allow representing three-dimensional object on a plane. On the diagrams the ventricular apex is displayed in the center, septum on the left, anterior, lateral and posterior walls - respectively at the top, right and bottom.

Input data for wavelet analysis method is sequence of $N$ three-dimensional distribution of radiopharmaceuticals, corresponding to $N$ intervals of “representative” cardiac cycle. These distributions are represented as $N$ polar diagrams of perfusion ($P_s$, $s = \overline{1,N}$), which are used for construction of sequence of wall thickening curves. Using approximation of the curves based on wavelet analysis, we obtain these functional images. As wavelet is considered complex B-spline wavelet with the following basal function:

$$\psi(t) = e^{2\pi i t}\frac{\sin((t/3)^3)}{(t/3)^3}.$$

### 4.2 Phase Images Construction

Let consider construction of phase polar diagram $\Phi$ on base of wavelet analysis. The wall thickening curve, corresponding distribution density of radiopharmaceuticals in myocardium at different $N$ intervals of cardiac cycle is constructed for finding element $(m,n)$ of the phase polar diagram $\Phi$. This wall thickening curve is a graph of a periodic function $f(t)$, whose values are known at $N$ points ( $f_s$=$P_s(m,n)$, $s = \overline{1,N}$). Wavelet series of the function is defined as follows:

$$F(t) = Re(\sum_{J,K} C_{JK}\psi_{JK}(t)), \tag{4}$$

where $\psi_{JK} = 2^{-J/2}\psi(2^{-J}t - K)$ ($J$ - scale, $K$ - displacement). Coefficients $C_{JK}$ are calculated by the formula

$$C_{JK} = \sum_{s=1}^{N} f_s {\psi^*}_{JK}(s-1),$$

where ${\psi^*}_{JK}$ is function, the complex conjugate of the function $\psi_{JK}$. After series of algebraic transformation formula ( 4) takes the following form

$$F(t) = (\sum_{J,K} A_{JK}\cos(2\pi(\frac{2^{-J}}{N}t - K) - \varphi_{JK})).$$

Coefficients $A_{JK}$ and $\varphi_{JK}$ are obtained using the following formulas

$$A_{JK} = \sqrt{{a_{JK}}^2 + {b_{JK}}^2},\ \varphi_{JK} = \arctan(\frac{b_{JK}}{a_{JK}}).$$

As result, elements of phase polar diagram $\Phi$ can be founded as

$$\Phi(m,n) = \frac{180}{\pi}\arctan(\frac{b_{JK}(m,n)}{a_{JK}(m,n)}).$$

For B-spline wavelet, coefficients $a_{JK}$ and $b_{JK}$ are calculated by formulas

$$a_{JK} = \sum_{s=1}^{N} P_s(m,n) 2^{-J} \frac{\sin(((\frac{2^{-J}(s-1)}{N} - K)/3)^3)}{((\frac{2^{-J}(s-1)}{N} - K)/3)^3} \times$$
$$\times \sin(2\pi(\frac{2^{-J}(s-1)}{N} - K)),$$

$$b_{JK} = \sum_{s=1}^{N} P_s(m,n) 2^{-J} \frac{\sin(((\frac{2^{-J}(s-1)}{N} - K)/3)^3)}{((\frac{2^{-J}(s-1)}{N} - K)/3)^3} \times$$
$$\times \cos(2\pi(\frac{2^{-J}(s-1)}{N} - K)).$$

Phase images of right ventricular (RV) based on Fourier analysis and wavelet analysis are represented on Fig. 12. Wavelet analysis using more accurate approximation of thickening curves allows getting more detailed phase images.

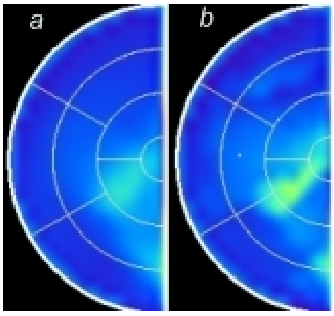

Figure 12. Phase images of RV are based on Fourier analysis ($a$) and B-spline wavelet ($b$).

## 4.3 Dyssynchrony Functional Images Construction

Let consider construction of functional images of systolic and diastolic dyssynchrony with using wavelet analysis. Algorithm of construction these images is represented on Fig. 13.

For finding element ($m$,$n$) of diagrams systolic dyssynchrony $SD$ and diastolic dyssynchrony $DD$, corresponding wall thickening curve is constructed on base of sequence of $N$ polar perfusion diagrams. Then this curve is approximated by wavelet analysis using following formula:

$$F(t) = \sum_{J_s K_s} A_{J_s K_s} \cos(2\pi(\frac{2^{-J_s}}{N} t - K_s) - \varphi_{J_s K_s}),$$

where $J_s$ and $K_s$ ($s = \overline{1,3}$) are set of scale parameters, which allow to get more accurate approximation of wall thickening curve. As result, the element ($m$,$n$) of diagram of systolic dyssynchrony $SD$ equals first intersection of graphs of approximation curve $F(t)$ and Fourier zero harmonic, which is interpreted as onset of mechanical contraction (OMC) [Chen et al., 2011].

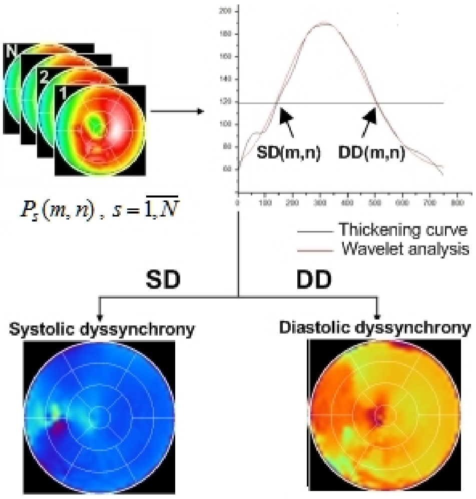

Figure 13. Functional images of systolic and diastolic dyssynchrony construction.

The element ($m$,$n$) of diagram of diastolic dyssynchrony $DD$ equals second intersection of these graphs. This value is interpreted as onset of mechanical relaxation (OMR) [Chen et al., 2011].

For comparative analysis we construct functional images with using Fourier analysis. In the case wall thickening curves are approximated by sum of the three harmonics Fourier [Hsu et al., 2013].

Functional images of diastolic dyssynchrony of LV on base wavelet analysis and 3-harmonic analysis are represented on Fig. 14. Phase analysis using wavelet functions can better approximate the variation of myocardial wall thickness over the cardiac cycle to calculate the OMC and OMR as measures of LV systolic and diastolic dyssynchrony.

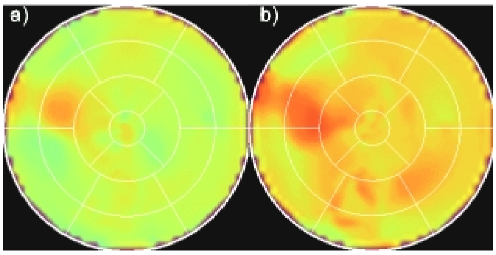

Figure 14. Functional images of diastolic dyssynchrony of LV are based on 3-harmonic phase analysis ($a$) and wavelet analysis ($b$).

## 5 Conclusion

Mathematical and software data processing of radionuclide studies allows defining a wide range of diagnostic parameters. Developed software is installed and tested in radioisotope laboratory of Central Clinical Hospital No. 2 named after Semashko OAO “RZD”, in “Federal Research Center of Transplantology and Artificial organs named after Academician V.I. Shumakov” and “Federal Research and Clinical Center of specialized types of health care and medical technology of the Federal Medical and Biological Agency” in Moscow.

## Acknowledgements

The authors acknowledge Saint-Petersburg State University for a research grant 9.38.673.2013.

## References

Arlychev, M.A., Novikov, V.L., Sidorov, A.V., Fialkovskii, A.M., Kotina, E.D., Ovsyannikov, D.A., and Ploskih, V.A. (2009) EFATOM two-detector one-photon emission gamma tomograph. *Technical Physics* **54**(10), pp. 1539–1547.

Balykina, Y.E., Kolpak, E.P., and Kotina, E.D. (2014) Mathematical model of thyroid function. *East Journal of Scientific Research* **19**(3), pp. 429–433.

Chen, Ji, Garcia, E.V., Folks, R.D., et al. (2005) Onset of left ventricular mechanical contraction as determined by phase analysis of ECG-gated myocardial perfusion SPECT imaging. *J. Nucl. Cardiol.* **12**(6), pp. 687–95.

Chen, Ji, Kalogeropoulos, A.P., Verdes, L., et al. (2011) Left-ventricular systolic and diastolic dyssynchrony as assessed by multi-harmonic phase analysis of gated SPECT myocardial perfusion imaging in patients with end-stage renal disease and normal LVEF. *J. Nucl. Cardiol.* **18**(2), pp. 299–308.

Dey, J., and King, M.A. (2009) Theoretical and Numerical Study of MLEM and OSEM Reconstruction Algorithms for Motion Correction in Emission Tomography. *IEEE Trans. Nucl. Sci.* **56**(5), pp. 2739–2749.

Eisner, R.L., Noever, T., Nowak, D., et al. (1987) Use of cross-correlation function to detect patient motion during SPECT imaging. *J. Nucl. Med.* **28**, pp. 97–101.

Elizarova, M.V., Ovsyannikov, D.A., and Cheremisin, V.M. (2007) Physical and technical aspects of radiation therapy. *Medical Physics. Information Technology*, p. 183.

Germano, G., Chua, T., Kavanagh, P., et al. (1993) Detection and correction of patient motion in dynamic and static myocardial SPECT using a multi-detector camera. *J. Nucl. Med.* **34**, pp. 1394–1395.

Hsu, T.H., Huang, W.S., Chen, C.C., et al. (2013) Left ventricular systolic and diastolic dyssynchrony assessed by phase analysis of gated SPECT myocardial perfusion imaging: a comparison with speckle tracking echocardiography. *Ann. Nucl. Med.* **27**, pp. 764–771.

Hudson, M., and Larkin, R.S. (1994) Accelerated Image Reconstruction using Ordered Subsets of Projection Data. *IEEE Trans. Med. Imag.* **13**, pp. 601–609.

Kotina, E.D. (2012) Data processing in radionuclide studies. *Problems of Atomic Science and Technology* **79**(3), pp. 195–198.

Kotina, E.D., Latypov, V.N., and Ploskikh, V.A. (2013) Universal System for Tomographic Reconstruction on GPUs. *Problems of Atomic Science and Technology* **6**(88), pp. 175–178.

Kotina, E.D., Maximov, K.M. (2011) Motion correction in planar and tomographic radionuclide studies. *Vestnik St. Petersburg University* **10**(1), pp. 29–36.

Kotina, E.D., Ostroumov, E.N., and Ploskikh, V.A. (2012) Left and Right Ventricular Phase Analysis of Gated SPECT Myocardial Perfusion. *European Journal of Nuclear Medicine and Molecular Imaging* **39**(2), p. 213.

Kotina, E.D., and Ploskikh, V.A. (2012) Data Processing and Quantitation in Nuclear Medicine. *Proceedings of RuPAC 2012*, pp. 526–528.

Kotina, E.D., Ploskikh, V.A., and Babin, A.V. (2013) Radionuclide Methods Application in Cardiac Studies. *Problems of Atomic Science and Technology* **6**(88), pp. 179–182.

Munshi, A. ed. (2014) The OpenCL Specification ver. 2.0. Khronos Group. *http://www.khronos.org/registry/cl/.* Last accessed 29 August.

Ostroumov, E.N., Kotina, E.D., Slobodyanik, V.V., et al. (2011) ECG-synchronized myocardial perfusion tomoscintigraphy and cardiac resynchronization therapy. *Russian Journal of Cardiology* **3**, pp. 58–65.

Ovsyannikov, D.A., and Kotina, E.D. (2012) Determination of velocity field by given density distribution of charged particles. *Problems of Atomic Science and Technology* **3**(79), pp. 122–125.

Ovsyannikov, D.A., Kotina, E.D., and Shirokolobov, A.Yu. (2013) Mathematical methods of motion correction in radionuclide studies. *Problems of atomic science and technology* **88**(6), pp. 137–140.

Pissanetzky, S. (1984) Sparse Matrix Technology. *Academic Press*, London.

Sarkar, S, Oghabian, M.A., Mohammadi, I., et al. (2007) A Linogram/Sinogram Cross-Correlation Method for Motion Correction in Planar and SPECT Imaging. *IEEE Transactions on nuclear science* **54**(1).

Shepp, L.A., and Vardi, Y. (1982) Maximum Likelihood Reconstruction for Emission Tomography. *IEEE Trans. Med. Imag.* **1**(2), pp. 113–121.

Shirokolobov, A.Yu. (2014) Mathematical Data Processing of Hepatobiliary Scintigraphy with a Motion Correction. *IEEE Proceedings of ICCTPEA-2014*, Saint-Petersburg, Russia, June 30–July 04, pp. 164–165.

Taylor, K., and Grant, G. (2006) Automated quantification of myocardial ischemia and wall motion defects by use of cardiac SPECT polar mapping and 4-dimensinonal surface rendering. *J. Nucl. Med. Technol.* **34**, pp. 3–17.